Journal of Photochemistry & Photobiology, B: Biology 198 (2019) 111594

Contents lists available at ScienceDirect

Journal of Photochemistry & Photobiology, B: Biology

journal homepage: www.elsevier.com/locate/jphotobiol

Synthesis, characterization, and supramolecular architectures of two distinct classes of probes for the visualization of endogenously generated hypochlorite ions in response to cellular activity

Richa Yadav[a,1], Keiko Odera[b,1], Abhishek Rai[a,2], Ryoya Takahashi[b,*], Lallan Mishra[a,*]

[a] Department of Chemistry, Institute of Science, Banaras Hindu University, Varanasi 221005, India
[b] Department of Biochemistry, Faculty of Pharmaceutical Sciences, Toho University, 2-2-1 Miyama, Funabashi, Chiba 274-8510, Japan

ARTICLE INFO

Keywords:
Supramolecule
Hypochlorite
Endosomes
Phagosomes

ABSTRACT

Two distinct classes of compounds, (E)-2-(((3-amino-4-nitrophenyl) imino) methyl)-5-(diethylamino) phenol (**SB**) and 5-(diethylamino)-2-(5-nitro-1H-benzo[*d*]imidazol-2-yl) phenol (**IM**) were synthesized. **SB**, a bright red colored compound was crystallized in acetonitrile as a triclinic crystal system while **IM**, yellow colored compound crystallized as a monoclinic crystal system in dimethylformamide by vapor diffusion of diethylether. These compounds were characterized using spectroscopic techniques (IR, UV–visible, ^{1}H, and ^{13}C NMR), and X-ray crystallography. **SB** and **IM** displayed classical and non-classical H-bonding involving C-H…O and π…π interactions. These compounds detected hypochlorite ions in aqueous DMSO (1: 9, *v*/v, HEPES buffer, pH 7.4), and detection was visible via color changes by naked eye. We also performed UV–visible and fluorescence titrations, showing detection limits of 8.82×10^{-7} M for **SB** and 2.44×10^{-7} M for **IM**. The fluorometric responses from **SB** and **IM** were also studied against different ROS and anions. DFT calculations were performed to strengthen the proposed sensing mechanisms of both **SB** and **IM**. Hypochlorite, which is endogenously generated by myeloperoxidase in endosomes, was specifically visualized using **SB** and **IM** in lipopolysaccharide-treated RAW264.7 cells. These probes were also used to image the generation of hypochlorite by RAW264.7 cells during phagocytosis of non-fluorescent polystyrene beads.

1. Introduction

Molecular recognition is a process by which molecules select and interact to each other governed by complementarity and forms an integral part of host–guest chemistry. To explore the treasure of molecular recognition principles for the detection of reactive oxygen species (ROS) is challenging at the cellular level [1]. Therefore, design and synthesis of receptors for detection of ROS is a demanding area of modern research. Among ROS, the hypochlorite ion targets multiple biological components including DNA, lipids, cholesterol, and proteins [2]. The oxidizing power of hypochlorite enables it to act as an antimicrobial agent capable of killing a variety of pathogens in living organisms [3]. Hypochlorite is generated endogenously by peroxidation of chloride ions; this process is catalyzed by the heme enzyme myeloperoxidase (MPO) via the MPO-H_2O_2-chloride system [4–6]. MPO is the only mammalian enzyme that produces hypochlorous acid or hypochlorite ion, ClO^-, under relevant physiological conditions [6,7]. Hypochlorite ion is also induced by microbial products, such as lipopolysaccharide (LPS), which is one of the major bacterial virulence factors with proinflammatory properties. However, abnormal overproduction of ClO^- can cause tissue damage and lead to oxidative stress, which is associated with cardiovascular diseases [8], inflammatory diseases, arthritis [9], kidney disorders [10] and several other life-threatening conditions [11]. Nature maintains a balance in all living organisms; endogenously-generated oxidative stress is counteracted by a low-molecular-weight antioxidant glutathione (GSH) [12]. GSH is abundantly generated in vivo to maintain the redox homeostasis of cells and tissues and to protect the essential components of the cells. This complex redox biology of the cell governs essential biological processes and has broad implications in human health [13]. Nevertheless, the biological activities of ClO^- have not been fully elucidated, highlighting the necessity to design probes for the detection and

* Corresponding authors.
E-mail addresses: takahasi@phar.toho-u.ac.jp (R. Takahashi), lmishrabhu@yahoo.co.in (L. Mishra).
[1] Both authors contributed equally to the work.
[2] Current address: Department of Chemistry, Kunwar Singh College (A constituent unit of L. N. Mithila University) Laheriasarai, Darbhanga, Bihar 846003, India.

https://doi.org/10.1016/j.jphotobiol.2019.111594
Received 19 March 2019; Received in revised form 23 July 2019; Accepted 13 August 2019
Available online 14 August 2019
1011-1344/

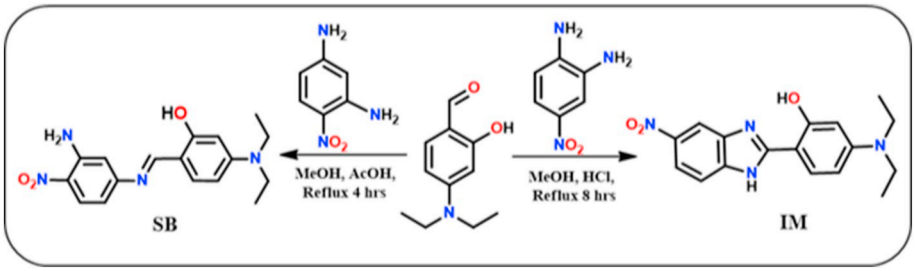

Scheme 1. Synthesis strategy for **SB** and **IM.**

squantification of ClO^- under physiological conditions; such probes would help us understand the biological redox cycle.

Several methods, including colorimetry, fluorimetry, electrochemical approaches, and chromatography, allow for the detection of hypochlorite ions [14–16]. Fluorescence spectrophotometry is used most because of its enhanced sensitivity, applicability, high resolution, and ability to conduct detection in real time [17,18]. Several dye-based fluorescent receptors, including cyanine, fluorescein, rhodamine, BODIPY, naphthalimide, and dicyanomethylene-4H-pyran, are also used to detect hypochlorite ions [19–25]. However, these fluorescent receptors show limited stability towards oxidants, are costly, require multistep synthesis and are obtained in low yields; once more highlighting the need for new fluorescent probes that are economic cost wise and easy to synthesize for hypochlorite ion detection [26,27].The compounds **SB** and **IM** presented here overcome these limitations as they give high yields in one pot reaction.

In this report, we focused on two compounds for recognition of hypochlorite ions; the structures of these compounds are illustrated in Scheme 1. One is a Schiff base while the second one is an imidazole. Schiff base are known for their wide applicability ranging from its use as catalysts, stabilizers, dyes, organic intermediates [28,29] to its potent biological role as antiviral, antimalarial, antifungal, antibacterial, antiproliferative, antipyretic agents [30–33]. Similarly, imidazole is also documented for their biological importance and sensing properties towards anions but less work is done on studying its interaction with ROS particularly hypochlorite ions [34–37]. Derivatives of 4-diethylaminosalicylaldehyde (DEA) show good spectral properties, biocompatibility, and ability to penetrate cellular membrane, rendering these compounds usable as fluorescent probes [38,39]. In this study, we investigated the use of **SB** and **IM** for the detection of hypochlorite ions under physiologic conditions.

2. Experimental Section

2.1. Materials and Methods

All the solvents were obtained from commercial sources and were dried and distilled prior to their use. The chemicals (4-nitro-*m*-phenylenediamine and 4-nitro-*o*-phenylenediamine) were purchased from Alfa Aesar, India and 4-diethylaminosalicylaldehyde from Sigma Aldrich, India. Infrared spectra were recorded at room temperature (303 *K*) using KBr pellets on a Varian 3300 FT-IR spectrophotometer, USA. UV–visible spectra were recorded on a Shimadzu UV-1601 spectrophotometer, Japan, and fluorescence spectra were measured on a PerkinElmer LS 55 Fluorescence spectrophotometer, USA at room temperature (303 K). The solvent system for all the absorbance and emission experiments was an aqueous DMSO (1: 9, v/v, HEPES buffer, 1×10^{-3} M, pH 7.4). The NMR spectra (^{1}H and ^{13}C) were collected on a JEOL AL500 FT-NMR spectrometer, USA, at room temperature (303 K). The chemical shifts (δ, ppm) were normalized to that of tetramethylsilane ($Si(CH_3)_4$) used as internal standard. Electro spray ionization mass spectrometry (ESI-MS) experiments were performed on Bruker Daltonics amaZon SL Max ion trap mass spectrometer, USA and Agilent Technologies 6530Accurate-Mass Q-TOF LC/MS unit, USA. X-ray diffraction data were collected by mounting a single crystal of sample on the glass fiber of an Agilent Technologies Oxford diffraction XCALIBUR-EOS diffractometer, USA. Monochromated MoKα radiation (λ = 0.71073 Å) was used for the measurements. The crystal structure was solved by using structure solution by direct methods using SHELXS-2014 program 7, and was refined using full matrix least squares (SHELXL-2014) [40]. The interaction of ClO^- with probes **SB** and **IM** was supported by energy-optimized structures at B3LYP level with basis sets 6-31G (d,p) and 6–31 (+ +) G (d,p) using Gaussian 09 program [41]. RAW264.7 cells were obtained from DS Pharma Biomedical, Japan. Fluorescent signals in cells were monitored using an inverted fluorescent microscope (Carl Zeiss Axio Vert.A1 FL-LED, Germany).

2.2. Synthesis of *SB*

A solution of 4-diethylaminosalicylaldehyde (0.193 g, 1.0×10^{-3} mol) in 10 mL methanol was refluxed together with a solution of 4-nitro-*m*-phenylenediamine (0.153 g, 1.0×10^{-3} mol) in 10 mL methanol for 4 h in the presence of two drops of glacial acetic acid. The bright red colored precipitate thus obtained was filtered and washed with diethyl ether and dried in vacuum. The product was recrystallized in acetonitrile. The crystals of **SB** suitable for X-ray measurements were grown by slow evaporation of a solution of **SB** in acetonitrile at room temperature. The obtained yield for **SB** = 86% (0.282 g). The values for FT-IR (KBr; cm^{-1}) were as follows: 3426, 3334, 2973, 1609, 1570, 1515, 1478, 1434, 1382, 1321, 1235, 1140, 1074, 1009, 960, 843, 818, 781, 749, 690, 571, 453. The values for ^{1}H NMR (500 MHz, DMSO-d_6) were as follows: δ 13.30 (s, broad, 1H, OH), 8.66 (s, 1H, HC═N), 7.98 (d, 1H, J = 8.5 Hz, phenyl), 7.44 (broad, 2H, NH_2), 7.34 (d, 1H, J = 8.5 Hz, phenyl), 6.76 (d, 1H, J = 2 Hz, phenyl), 6.55 (q, 1H, Ar), 6.33 (d, 1H, J = 8 Hz, phenyl), 6.05 (d, 1H, J = 2 Hz, phenyl), 3.39 (t, 4H), 1.10 (q, 6H). The values for ^{13}C NMR (125 MHz, DMSO-d_6) were as follows: 164.49 (-C-OH), 163.16 (-HC=N), 154.99, 128.43, 127.72, 110.19, 109.47, 109.04, 105.05, 97.20, 44.56 (-CH_2), 13.07 (-CH_3). The values for ESI-MS calculated for $C_{17}H_{20}N_4O_3$ $[M + H]^+$ were as follows: 329.1614, found: 329.1615; crystal system, triclinic; space group, P-1; a (Å),7.1633(3); b (Å), 8.1894(4); c (Å), 15.4615(9); α (°), 102.288(4); β (°), 94.259(5); γ (°), 111.069(3); volume ($Å^3$), 815.61(7); Z = 2.

2.3. Synthesis of *IM*

In our present study, **IM** was prepared as a control compound using a slight modification to reported method [42]. **IM** was characterized using X-ray crystallography. In this study, we used a solution of 4-diethylaminosalicylaldehyde (0.289 g, 1.5×10^{-3} mol) in 10 mL methanol; this was added under stirring to a solution of 4-nitro-*o*-phenylenediamine (0.153 g, 1.0×10^{-3} mol) in methanol (10 mL) in the presence of two drops of HCl. The resulting solution was refluxed for 8 h. The progress of the reaction was monitored by TLC. The reaction mixture was then cooled to room temperature. The obtained yellow-colored precipitate was filtered using a vacuum pump, washed twice with 2 mL (each) of diethyl ether, and dried under vacuum. **IM** crystals

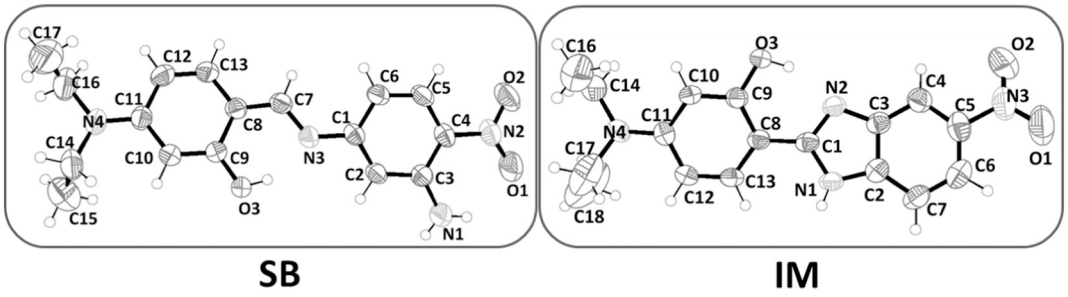

Fig. 1. Molecular structure (ORTEP) of **SB** and **IM** drawn at 50% probability level.

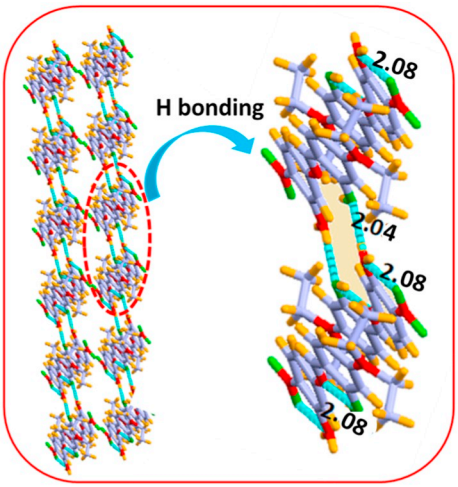

Fig. 2. Packing diagram of **SB** generated via H-bonded interactions. Light violet, red, and green represent carbon, nitrogen, and oxygen atoms, respectively. (For interpretation of the references to color in this figure legend, the reader is referred to the web version of this article.)

suitable for X-ray measurements were grown by slow vapor diffusion of diethyl ether over a saturated solution of **IM** in dimethylformamide (DMF) at room temperature. The obtained yield = 81% (0.264 g). The values for FT-IR (KBr; cm^{-1}) were: 3321, 1645, 1589, 1556, 1502, 1470, 1446, 1426, 1359, 1339, 1266, 1213, 1143, 1084, 818, 786, 732, 600. The values for ^{1}H NMR (500 MHz, DMSO-d_6) were: δ 13.12 (s, broad, 1H, -OH), 12.36 (s, broad, 1H, -NH), 8.38 (s, 1H, -phenyl), 8.10 (d, 1H, J = 8.5 Hz, -phenyl), 7.84 (d, 1H, J = 8.5 Hz, −phenyl), 7.68 (d, 1H, J = 8.5 Hz, -phenyl), 6.42 (d, 1H, J = 9 Hz, -phenyl), 6.22 (s, 1H), 3.40 (q, 4H), 1.14 (t, 6H). The values for ^{13}C NMR (125 MHz, DMSO-d_6) were: 13.44, 44.78, 98.47, 100.61, 104.96, 118.74, 129.06, 143.13, 151.96, 157.91, 160.92. The values for ESI-MS calculated for $C_{17}H_{18}N_4O_3$ $[M + H]^+$ were: 327.1458, found: 327.1459; crystal system, monoclinic; space group, C 2/c; a (Å), 13.737(11); b (Å), 6.740(6); c (Å), 34.07(3); α (°), 90.00; β (°), 101.15(2); γ (°), 90.00; volume ($Å^3$), 3095(4); Z = 8.

2.4. UV–Visible and Fluorescence Spectra

For all the spectral studies, stock solutions of **SB** and **IM** were prepared separately in DMSO (1.0×10^{-3} M). The stock solutions (1.0×10^{-2} M) of F^-, Cl^-, Br^-, CN^-, N_3^-, OH^-, NO_3^-, NO_2^-, AcO^-, PO_4^{3-}, and S^{2-} were prepared separately by dissolving the corresponding salts in double-distilled water for individual additions. The concentration of hypochlorite (ClO^-) was determined using an extinction coefficient of 350 M^{-1} cm^{-1} (λ_{max} 292 nm) at pH 9.0 [43]. The hydroxyl radical ($^{\bullet}OH$) was generated by Fenton reaction between H_2O_2 and aqueous solution of ferrous ammonium sulphate [44]. Superoxide ($O_2^{\bullet -}$) was generated from sodium hydroxide and hydrogen peroxide [45]. The concentration of commercially available stock solution of H_2O_2 was determined from its absorbance at λ_{max} 240 nm [46]. Peroxynitrite ($ONOO^-$) was prepared using a method reported previously [47]. The concentration of $ONOO^-$ was determined using an extinction coefficient of 1670 M^{-1} cm^{-1} (λ_{max} 302 nm). Singlet oxygen ($^1O_2$) was obtained by the addition of an aqueous solution of NaClO to H_2O_2 using a method reported previously [48]. The stock solutions of **SB** and **IM** were then diluted separately to a concentration of 1.0×10^{-5} M with the addition of aqueous DMSO (1: 9, *v*/v, HEPES buffer, 1×10^{-3} M, pH 7.4). For absorption and fluorescence measurements, 3.0 mL of each solution of **SB** and **IM** was placed into a quartz cell having 1×10^{-2} m optical path length, and the spectra were recorded at room temperature. The excitation and emission slit widths were maintained at 10 nm. The excitation wavelengths for the measurement of fluorescence spectra were set to λ_{exct} = 438 nm and λ_{exct} = 415 nm for **SB** and **IM**, respectively. For titrations, a solution of corresponding ion was gradually added into the solution of **SB** or **IM** at a fixed fraction using a micropipette, and was mixed thoroughly using micropipette before recording the spectra.

2.5. ^{1}H NMR Titrations

NMR titrations were carried out by incremental addition of ClO^- (in D_2O) to the solution of **SB** (DMSO-d_6) and to that of **IM** (DMSO-d_6).

2.6. Determination of Detection Limit

The limit of detection (LOD) for probes **SB** and **IM** with respect to ClO^- was calculated using the results of fluorometric titrations. To ascertain the S/N ratio, emission intensity from **SB** and **IM** in the presence of ClO^- was determined 10 times, and standard deviation of the working curve was calculated. The LOD was then obtained using the formula, LOD = 3δ/k, where δ refers to the standard deviation of blank measurement, and k is the slope of the best fitted line [49].

2.7. Cell Culture

RAW264.7 cells (DS Pharma Biomedical, Japan) were maintained in DMEM (1.0 g/L glucose supplemented with sodium pyruvate, without L-Gln or Phenol Red) (Nacalai Tesque Inc., Japan) containing 10% heat-inactivated fetal bovine serum (Gibco, Australia), 2 mmol/L L-Ala-L-Gln, 100 U/mL penicillin, and 100 U/mL streptomycin, under a humidified atmosphere of 95% air and 5% CO_2 at 37 °C.

2.8. Hypochlorite Imaging in PMA- and LPS-Treated Cells

RAW264.7 cells were plated at 10,000 cells per well, in 100 μL media per well, in a 96-well black-wall clear-bottom culture microplate (EZVIEW glass bottom culture plate LB; IWAKI, Japan), and were allowed to attach to the wells. The cells were then treated for 24 h with 1.0×10^{-6} M phorbol 12-myristate 13-acetate (PMA) or 1.0×10^{-7} g/mL lipopolysaccharide (LPS from *E. coli* O111:B4, Sigma-Aldrich). For fluorescence imaging of endogenous hypochlorite generation in PMA-

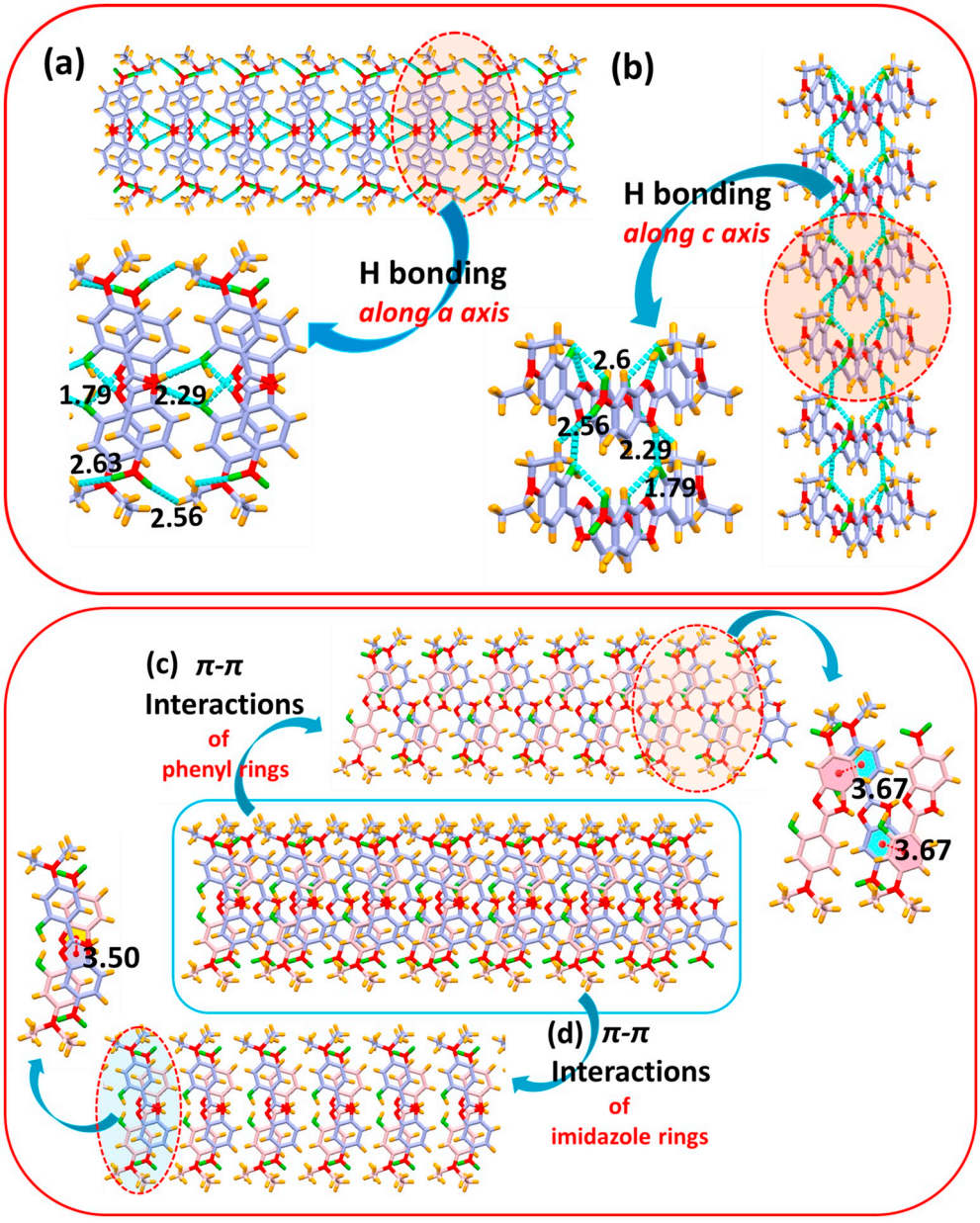

Fig. 3. Packing of **IM** via: (a) H-bonding along crystallographic a-axis, (b) H-bonding along crystallographic c-axis, (c) π-π interactions of the two phenyl rings at a centroid distance of 3.67 Å, (d) π-π interactions of imidazole rings at a centroid distance of 3.50 Å.

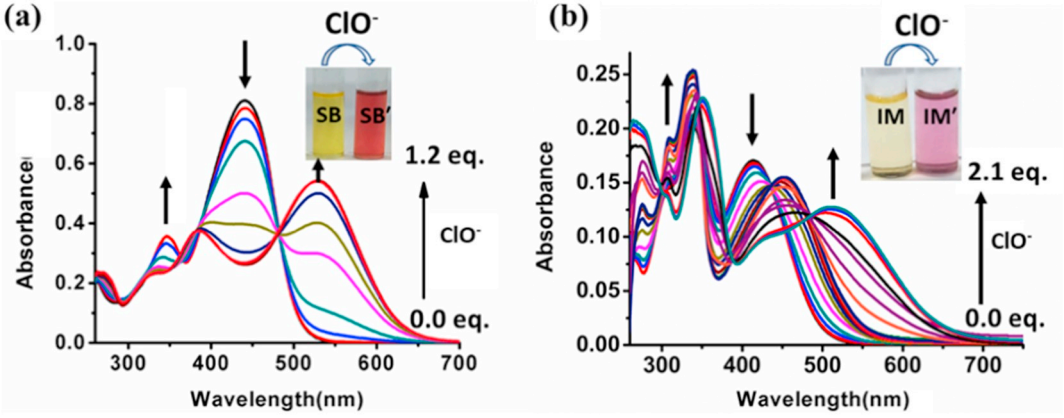

Fig. 4. UV–visible titrations of: (a) **SB** (1.0×10^{-5} M) and (b) **IM** (1.0×10^{-5} M) in aqueous DMSO (1: 9, v/v, HEPES buffer, 1×10^{-3} M, pH 7.4) using incremental addition of aqueous solution of NaOCl. Inset: color change exhibited by the probes in the presence of ClO^- under normal light.

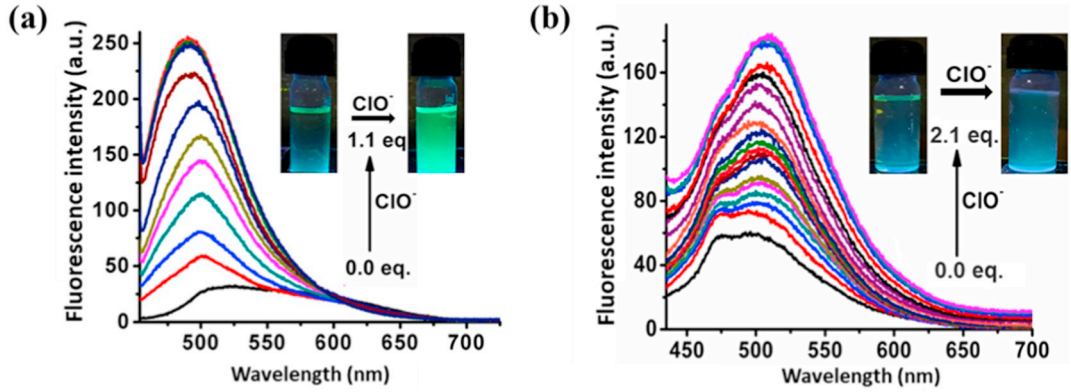

Fig. 5. Fluorescence titrations of: (a) **SB** (1.0×10^{-5} M) and (b) **IM** (1.0×10^{-5} M) in aqueous DMSO (1: 9, *v*/v, HEPES buffer, 1×10^{-3} M, pH 7.4) using incremental addition of aqueous solution of NaOCl. Inset: color changes in probes in the presence of ClO^- under UV lamp.

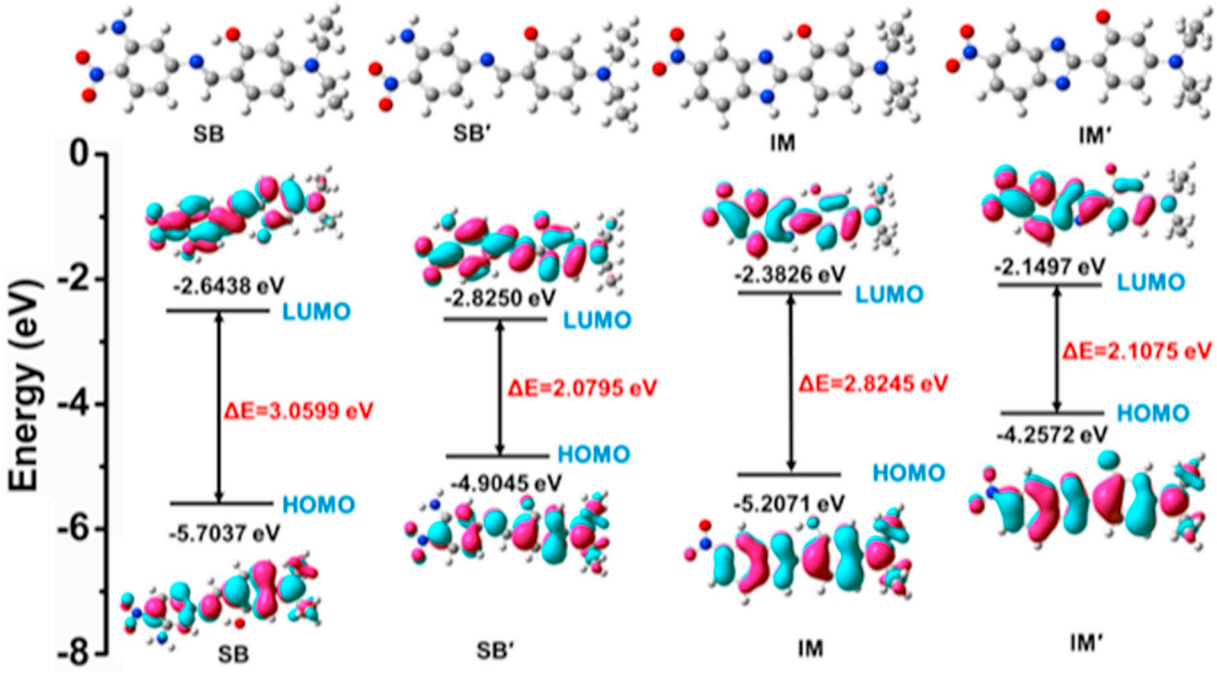

Fig. 6. DFT optimized minimum energy structures of **SB**, **SB′** (oxidized **SB**) and **IM, IM′.**

and LPS-stimulated cells, the cells were washed twice with phosphate buffered saline (PBS) and incubated with 5.0×10^{-6} M hypochlorite probe (**SB** or **IM**) in PBS.

Fluorescence signals in cells were monitored using an inverted fluorescence microscope (Axio Vert.A1 FL-LED, Carl Zeiss Microscopy GmbH, Germany) using a 40× EC Plan-Neofluar objective. Detection of fluorescence using **SB** and **IM** was conducted using a Zeiss Filter Set 38 (excitation BP 470/40, beam splitter FT 495, emission BP 525/50). Images were captured using a Zeiss AxioCam MRm camera and further processed using AxioVision 4.8.2 (Carl Zeiss) and ImageQuant TL (GE Healthcare Japan Corp., Japan) software.

2.9. Inhibition of Endogenous Hypochlorite Generation in Cells

Inhibition of endogenous hypochlorite generation in cells was performed using a specific inhibitor of myeloperoxidase (4-aminobenzoic acid hydrazide, ABAH) [50] and hypochlorite quenchers GSH [51] and taurine [52]. PMA- and LPS-treated cells were pretreated with 0.1×10^{-3} M ABAH, 5.0×10^{-3} M GSH, and 5.0×10^{-3} M taurine for 2 h. The cells were then washed with PBS and incubated with 5.0×10^{-6} M hypochlorite probe (**SB** or **IM**) in PBS containing each inhibitor. Fluorescent signals in cells were monitored using an inverted fluorescent microscope (Carl Zeiss) as described above.

2.10. Phagocytosis Assay

LPS-stimulated RAW264.7 cells were allowed to internalize 1-μm non-fluorescent polystyrene beads (Polybead Polystyrene Microspheres, Polysciences Inc., USA) for 30 min. The cells were then washed with PBS and incubated with 5.0×10^{-6} M hypochlorite probe (**SB** or **IM**). Fluorescent signals in the cells were monitored using an inverted fluorescent microscope (Carl Zeiss) as described above.

3. Results and Discussion

3.1. Synthesis and Characterization of *SB* and *IM*

The synthesized compounds **SB** and **IM** contain two components: an electron-donating diethylamino group in a framework of a phenolic ring, and an electron-withdrawing nitro group in a frame of aniline. In **SB,** these two components are connected via an imino group. In **IM**, the electron-donating group is directly connected to a nitrobenzimidazole

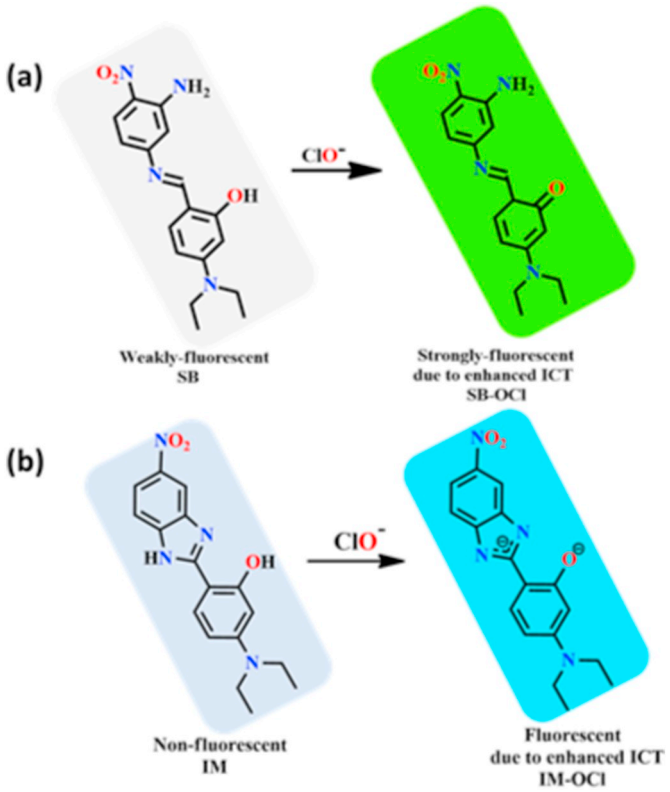

Fig. 7. Proposed sensing mechanism of **SB** and **IM** with respect to ClO^-.

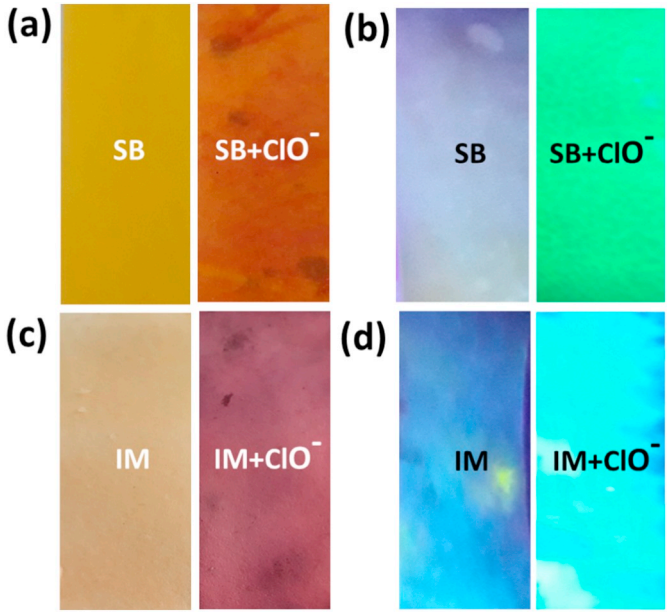

Fig. 8. Color changes of **SB**-loaded paper strips in the presence of ClO^- under daylight (a) and UV light (b) color changes of **IM**-loaded paper strips in the presence of ClO^- under daylight (c) and UV light (d).

ring system. The strategically designed frameworks of **SB** responded robustly to the biologically relevant hypochlorite ions. To comparatively assess the recognition properties of **SB**, we synthesized another distinct compound, **IM**, which bears a biologically relevant imidazolyl group.

The two compounds were fully characterized using IR, ^1H and ^{13}C NMR, UV–visible, fluorescence spectra, and ESI-MS (Figs. S1-S7†), and were authenticated by X-ray crystallography using a single crystal of each compound. The IR spectrum of **SB**, displayed a prominent peak at 1609 cm^{-1}, attributed to υ (CH=N) vibration. Other peaks at 3426 cm^{-1} and 3334 cm^{-1} in the **SB** spectrum were assigned to υ (NH_2) vibrations, as shown in Fig. S1a†. The peaks observed at 3321 cm^{-1} and 1645 cm^{-1} in the IR spectrum of **IM** were assigned to υ NH and υ C=N vibrations of the imidazolyl ring, respectively (Fig. S1b†). In the ^1H NMR spectrum of **SB,** the peaks observed at δ 13.30 ppm and δ 8.67 ppm were assigned to –OH and –CH=N protons, respectively (Fig. S2†). The amino protons of **SB** were deshielded and displayed at δ 7.44 ppm. The deshielding was due to the presence of a neighbouring electron-withdrawing nitro group. A peak at δ 163.16 ppm, assigned to imine carbon, supported the formation of a Schiff base (Fig. S3†). As shown in Fig. S4†, the peaks observed at δ 13.12, 12.36, and 8.38 ppm in the ^1H NMR spectrum of **IM** were assigned to –OH, -NH protons, and the proton ortho to the nitro group, respectively. The ^{13}C NMR spectrum of **IM** is shown in Fig. S5†. The ESI-MS spectra of **SB** and **IM** displayed major peaks at *m/z* 329.1614 and m/z 327.1459, attributed to $[\mathbf{SB} + H]^+$ and $[\mathbf{IM} + H]^+$ respectively (Figs. S6-S7†). The molecular structures of **SB** and **IM** are shown in Fig. 1.

3.2. Crystal Structures and Supramolecular Architectures of the Probe *SB* and *IM*

The crystallographic parameters of **SB** and **IM** are provided in Table S1. The compound **SB** crystallized in a triclinic system with space group P-1. The interplanar angle between the two phenyl rings bearing an electron-releasing group N-$(C_2H_5)_2$ and an electron withdrawing nitro group, connected via an imine bond in **SB,** was observed as 12.66° (Fig. S11a). **SB** displays two intramolecular hydrogen bonds, one between the hydroxyl and imino group (O3-H3…N3), and the other between the amino group and nitro oxygen (N1-H1A…O1); this is shown in Fig. S8a†. Additionally, a strong intermolecular H bond was displayed between the amino nitrogen and the hydroxyl hydrogen (Fig. S8b†). There were two non-classical H-bonding interactions between C5-H5 of the phenyl ring and O2 of the nitro group, and between C17-H17C of the N-diethyl amino group and the O1 of the nitro group (Fig. S8c†). Additionally, π…π interactions were observed at a centroid distance of 4.02 Å between the phenyl rings containing the nitro group and the hydroxyl group. The parameters of these weaker interactions are provided in Table S2. The association of molecules via hydrogen bonding generated stringed supramolecular architecture, as depicted in Fig. 2.

In **IM**, an intramolecular H-bond (O3-H3…N2) was formed at a distance of 1.79 Å, whereas intermolecular H-bond formation (N1-H1…O3) occurred at a distance of 2.29 Å (Figs. S9a-b†). In addition to these classical H-bonds, a non-classical H-bond was also present between the $CH(CH_3)$ of one molecule and the oxygen atom of NO_2 in another molecule at a distance of 2.56 Å (Fig. S9c†). Additionally, a strong π…π interaction, at a distance of 3.67 Å, was observed between a phenyl ring containing a nitro group belonging to one molecule and a phenyl ring containing a diethylamino group belonging to another molecule (Fig. S9d†). A π…π interaction was also observed between the imidazole rings of two different molecules at a centroid distance of 3.50 Å (Fig. S9e†). The supramolecular structures, formed via hydrogen bonding along crystallographic axes a and c, as well as π…π interactions, are shown in Fig. 3. The overall supramolecular architecture involving all these non-covalent interactions generated a network of interconnected rings (Fig. S10†). The bond lengths and bond angles of **SB** and **IM** are provided in Table S3. The dihedral angles between the planes of **SB** and **IM** are separately shown in Fig. S11†.

3.3. Colorimetric Response of Probes *SB* and *IM* to Hypochlorite Ion

Visual inspection of probes **SB** and **IM** in aqueous DMSO (1: 9, *v*/v, HEPES buffer, 1×10^{-3} M, pH 7.4), in the presence of different anions and ROS (10 equivalents), showed color changes from yellow to dark

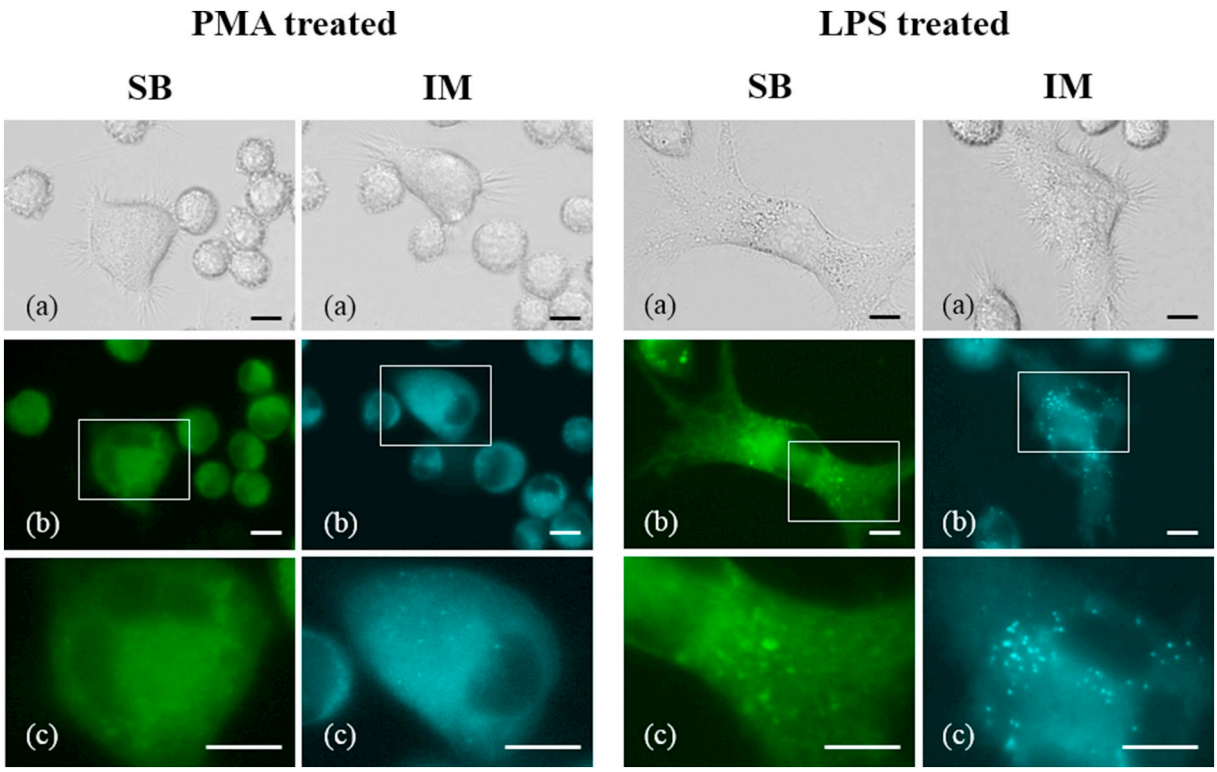

Fig. 9. Fluorescence images of PMA- and LPS-stimulated RAW264.7 cells incubated with hypochlorite probes **SB** and **IM**. PMA-treated RAW264.7 cells were incubated with 5×10^{-6} M **SB** (left) or **IM** (right). Bright field image (a), fluorescence image (b), and enlarged images of square area in b (c). Bars: 10 μm.

red and purple respectively, only with respect to hypochlorite ions (Figs. S12 and S13†). This prompted us to record the UV–visible spectra of **SB** and **IM**. **SB** displayed a strong band at λ_{max} 438 nm and a weaker band at λ_{max} 331 nm. Upon incremental addition of ClO^-, the peak observed earlier at λ_{max} 438 nm started to diminish with a red shift of 90 nm, and appeared at λ_{max} 528 nm (Fig. S14a†). Additional peaks were also observed at λ_{max} 271 nm and 383 nm. **SB** produced a color change from yellow to dark red in the presence of ClO^- ions, as shown in the inset of Fig. 4a. Other anions and ROS did not induce any appreciable changes in the color of (Fig. S12†) or spectra of **SB** (Fig. S14a†). Similarly, the peak observed at λ_{max} 415 nm in the spectra of free **IM** shifted to λ_{max} 523 nm, showing a bathochromic shift of 108 nm in the presence of ClO^- (Figs. 4b and S14b†). The other **IM** peak was retained at λ_{max} 337 nm. The color of **IM** changed from yellow to purple upon incremental addition of ClO^-, as shown in the inset of Figs. 4b and S13†.

3.4. Fluorometric Responses of *SB* and *IM* to Hypochlorite Ions

The fluorometric responses from **SB** and **IM** to various anions and ROS are shown in Figs. S15a-d†. However, **SB** and **IM** selectively detected only ClO^- with enhanced intensity of emission. The emission generated by free **SB** at λ_{em} 523 nm shifted to 491 nm, with intensity increased 10-fold upon the addition of ClO^-. The titrations of **SB** with ClO^- are depicted in Fig. 5a. The emissions generated by **IM,** initially observed at λ_{em} 476 nm and λ_{em} 495 nm, finally coalesced at λ_{em} 518 nm, with intensity increasing upon gradual addition of ClO^- as shown in Fig. 5b. The final changes in the color are depicted as insets in the corresponding figures.

3.5. pH Studies

pH-dependent variations in fluorescence, emitted by probes **SB** and **IM** in the absence and presence of ClO^-, are depicted in Fig. S16†. These results show that these probes are suitable for the detection of ClO^- in biological systems at physiological pH**.**

3.6. Response Time and Detection Limit

Response time is another important criterion for assessing the reliability of a fluorescent probe. As shown in Fig. S17†, an increase in fluorescence occurred within 60 s of adding ClO^- to **SB,** while the response of **IM** was relatively more rapid at 40 s. The interaction of the probe **SB** and **IM** with hypochlorite ions were also analysed quantitatively as depicted in the Figs. S18-S19†. A satisfactory linear relationship was observed with an acceptable correlation coefficient. These results indicate that **SB** and **IM** can be applied for the quantitative estimation of ClO^- using fluorometric spectroscopy (Fig. S18†). The detection limit of **SB** was 8.82×10^{-7} M (Fig. S19a†), and that of **IM** was 2.44×10^{-7} M (Fig. S19b†).

3.7. Interference and Competition Experiments

To assess whether **SB** and **IM** showed specificity only towards ClO^-, we measured the fluorometric responses of each probe to other anions and ROS; each probe was assessed in aqueous DMSO (1: 9, *v*/v, HEPES buffer, 1×10^{-3} M, pH 7.4). Other anions and ROS failed to trigger the increase in fluorescence intensity that was induced by ClO^- in each probe. The histograms in Figs. S20 and S21† show that ClO^- increased the emission of fluorescence notably more than did other analytes, indicating the high selectivity of probes towards ClO^-.

3.8. Computational Analyses

To understand the sensing mechanisms involved in the reactivity of **SB** and **IM** to ClO^-, we performed DFT calculations using the B3LYP/6-31G (d, p) or 6–31(++)G (d,p) method with the Gaussian 09 program. Orbital analysis revealed that in the highest occupied molecular orbital (HOMO), charge density in both **SB** and **IM** was mainly localized on the diethylamino moiety, whereas in the lowest unoccupied molecular

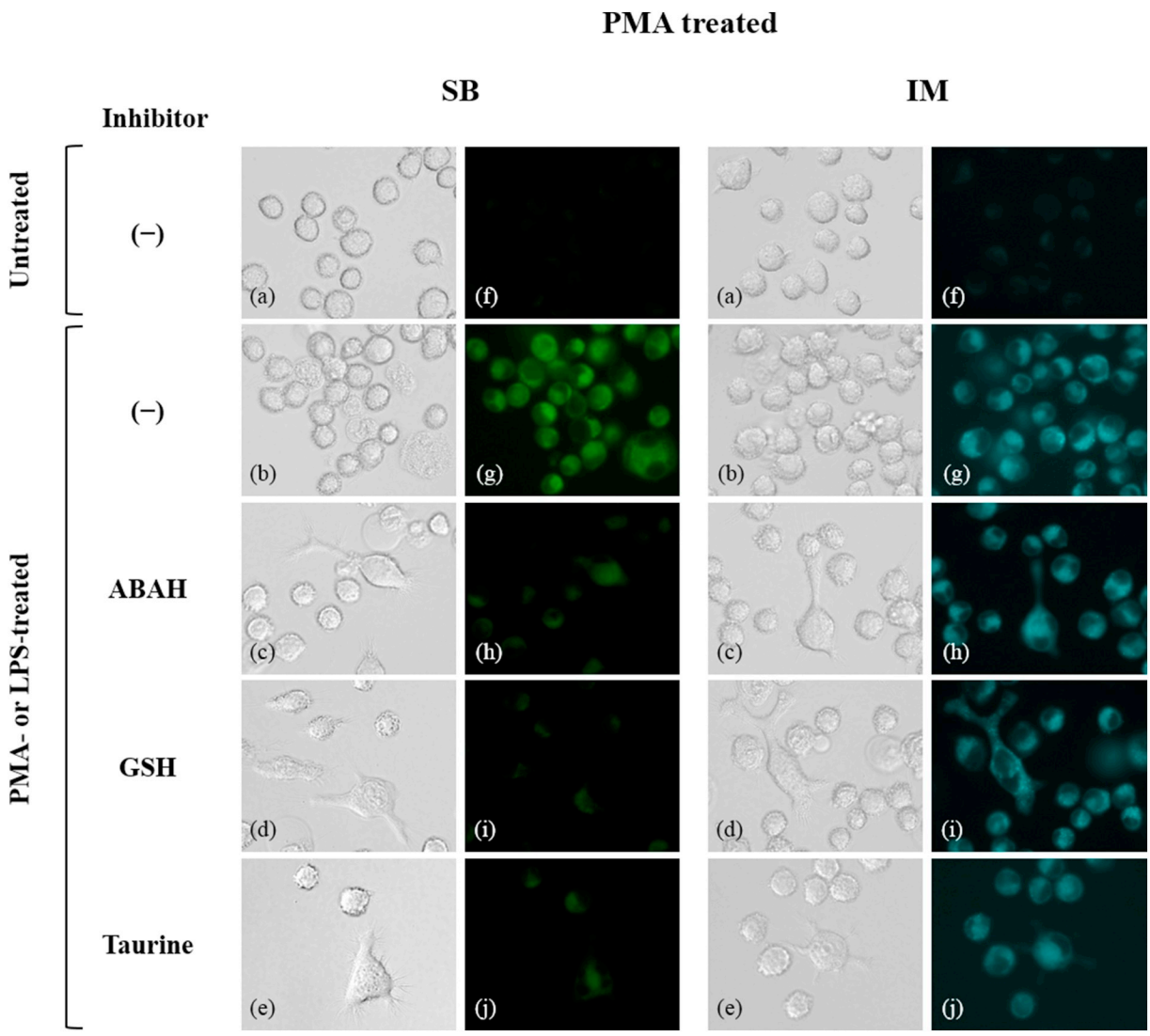

Fig. 10. Effects of myeloperoxidase inhibitor and hypochlorite scavengers on fluorescence intensity of **SB** and **IM** in PMA-treated RAW264.7 cells. PMA-untreated (a, f) and PMA-treated RAW 264.7 cells (b-e, g-j) were cultured for 2 h in the presence of 0.1×10^{-3} M ABAH (c, h), 5×10^{-3} M GSH (d, i), and 5×10^{-3} M taurine (e, j); this was followed by the addition of **SB** or **IM**. Bright-field images (a-e) and fluorescence images (f-j) of PMA-treated cells after incubation with 5×10^{-6} M **SB** or **IM**.

orbital (LUMO), charge density was localized on the nitrophenyl group (Fig. 6). Additionally, a decrease in molecular frontier orbitals energy supported the observed bathochromic effect in the UV–visible spectra of oxidized probes (**SB′** and **IM′**).

3.9. Proposed Mechanism

To investigate the sensing mechanism of ClO^- interacting separately with **SB** [53] and **IM,** ^{1}H NMR titrations, ESI-mass analysis and theoretical calculations were carried out. The ^{1}H NMR titrations of **SB** with incremental addition of ClO^- has been carried out as depicted in Fig. S22†). The phenolic OH proton of **SB** disappeared upon the addition of ClO^-, while NH_2 protons shifted from their original peak observed at δ 7.41 ppm to that at δ 7.37 ppm. The phenyl protons shifted upfield due to delocalization of negative charge throughout the organic framework of **SB**. These observations suggest that ClO^- oxidizes the hydroxyl proton generating fluorogenic oxidized **SB** (**SB′**), as shown in Fig. 7a. Further the change in chemical shift values of **SB** after addition of excess of ClO^- showing the emergence of a new proton signal at δ 2.92 ppm has been depicted in Fig. S23†. The mass spectrum of **SB′**, shown in Fig. S24†, showed a peak at m/z = 329.1595, which was assigned to $[\mathbf{SB'} + H]^+$ [54]. While in case of **IM**, the addition of ClO^-, leads to the deprotonation of the acidic protons **(**NH proton of the benzimidazole ring and OH proton of the salicylal group) accompanied by instant color change from yellow to purple and generates **IM′**. The formation of **IM′** has been supported by ^{1}H NMR titrations (Fig. S25†) and its mass spectrum (Fig. S26†) which showed a peak at m/z = 325.1256 assigned to $[\mathbf{IM'} + H]^-$. Thus, the two distinct classes of compounds (**SB** and **IM**) discussed here trace two different pathways for sensing hypochlorite i.e. oxidation and deprotonation respectively. The bathochromic shift that occurred in the absorbance spectra of both probes indicates intramolecular charge transfer (ICT) from the electron-rich center (diethylamino moiety) to the electron-deficient center (nitro group). Thus, based on above evidences the proposed sensing mechanism of probe **SB** and **IM** is shown in Fig. 7.

3.10. Ready-to-Use Paper Strips

To show how **SB** and **IM** probes can be used on test-paper strips for the detection of ClO^-, we used rectangular small paper strips (Whatman 1440–125 Ashless Quantitative Filter Paper, 8 Micron, Grade 40). These paper strips were dipped into a solution containing

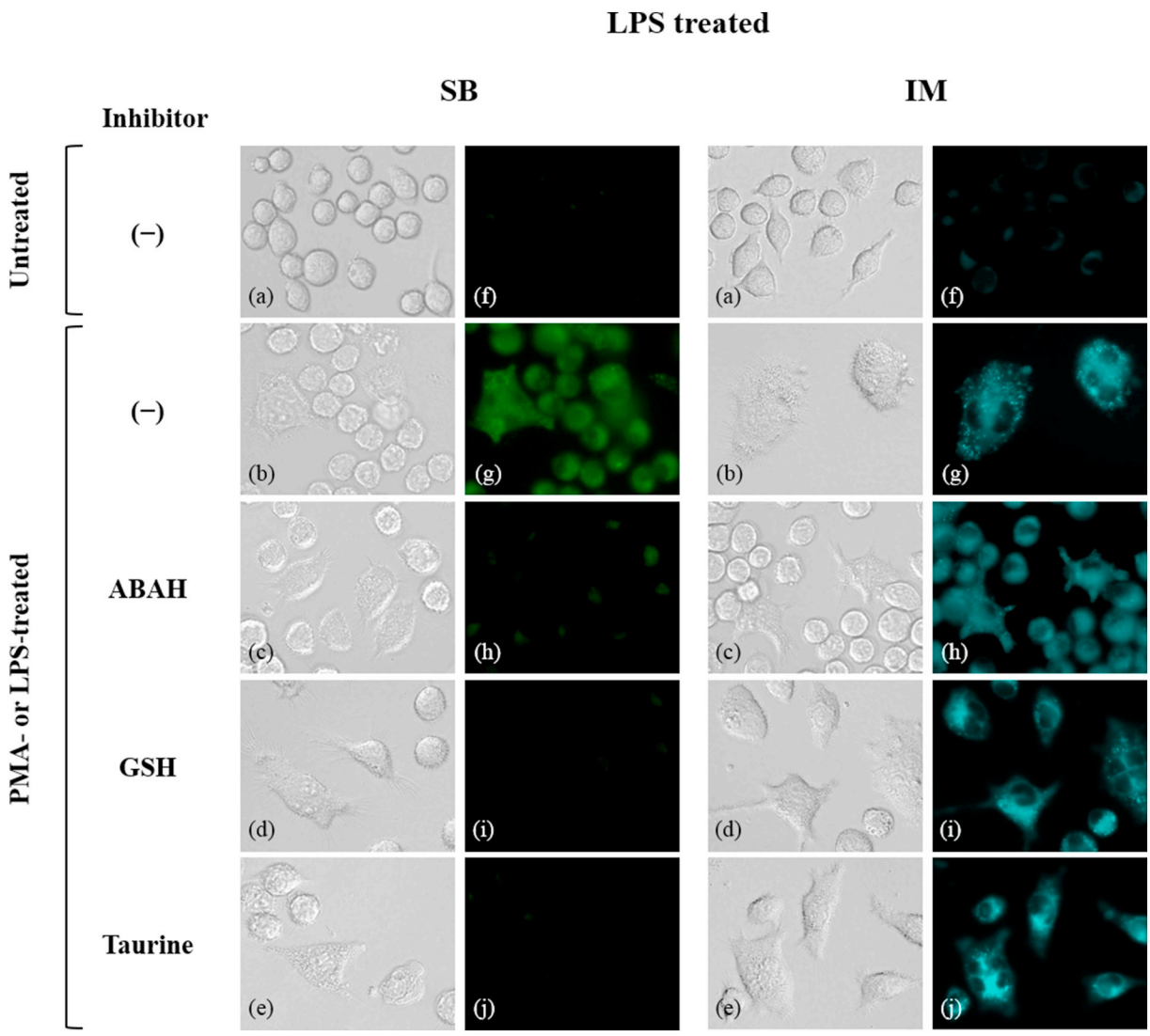

Fig. 11. Effects of myeloperoxidase inhibitor and hypochlorite scavengers on fluorescence intensity of **SB** and **IM** in LPS-treated RAW264.7 cells. LPS-untreated (a, f) and LPS-treated RAW 264.7 cells (b-e, g-j) were cultured for 2 h in the presence of 0.1×10^{-3} M ABAH (c, h), 5×10^{-3} M GSH (d, i), and 5×10^{-3} M taurine (e, j); this was followed by the addition of **SB** or **IM**. Bright-field images (a-e) and fluorescence images (f-j) of LPS-treated cells after incubation with 5×10^{-6} M **SB** or **IM**.

each respective probe (1.0×10^{-3} M) in aqueous DMSO (1: 9, *v*/v, HEPES buffer, 1×10^{-3} M, pH 7.4). The dried test-paper strips were then dipped into a solution of ClO^- (1×10^{-5} M in water) for 5 min, and air dried, and then visualized under daylight and UV light (365 nm). The color changes observed using these strips were similar to those obtained using probe solutions. This indicates that the **SB** and **IM** probes can be used on a solid cellulose surface to detect ClO^- (Fig. 8).

3.11. Imaging of Endogenously Produced Hypochlorite in PMA- and LPS-Treated RAW264.7 Cells

Macrophages stimulated with PMA and LPS increase their production of reactive oxygen species including that of ClO^-; however, the mechanisms of hypochlorite generation, stimulated by treatment with PMA or LPS, are different [55–58]. PMA activates NADPH oxidase and generate the production of ClO^- coupled with that of ROS [59]. LPS generates the production of ClO^- via MPO, other inducible gene products, and morphological alterations [60].

To investigate whether our hypochlorite-sensing probes **SB** and **IM** are usable in living cells, we imaged fluorescence triggered by the generation of ClO^- in RAW264.7 cells stimulated with PMA or LPS.

As shown in Fig. S27†, PMA induced squamous morphology with increased cytoplasmic volume in RAW264.7 cells. In contrast, LPS induced morphological changes in RAW264.7 cells, leading to increasing polarization of these macrophages from an undifferentiated rounded shape to an activated dendritic shape.

In PMA-treated cells, fluorescence signals emitted by **SB** and **IM** were observed diffusely throughout the cytoplasm (Fig. 9). Conversely, in LPS-treated cells, fluorescence signals emitted by **SB** and **IM** were observed as granule-like structures with uniform reduced fluorescence in the cytoplasm of the cells (Fig. 9). Previous studies [58–60] have shown that granule-like structures found in the cytoplasm of the cells are endosomes formed by stimulation with LPS. No significant fluorescence signals from **SB** or **IM** were detected in the nuclei of PMA- or LPS-treated RAW264.7 cells.

To assess the specificity of **SB** and **IM** probes in living cells, we investigated the effects of a myeloperoxidase inhibitor and hypochlorite scavengers in PMA- and LPS-treated RAW264.7 cells. As shown in Fig. 10 (left), the cells untreated with PMA showed barely detectable background-fluorescence signals. Pretreating PMA-stimulated RAW264.7 cells with ABAH (which inhibits production of hypochlorous acid by myeloperoxidase) significantly decreased the fluorescent signal emitted by the **SB** probe compared with that in corresponding PMA-stimulated control RAW264.7 cells not treated with the inhibitor. Treating PMA-

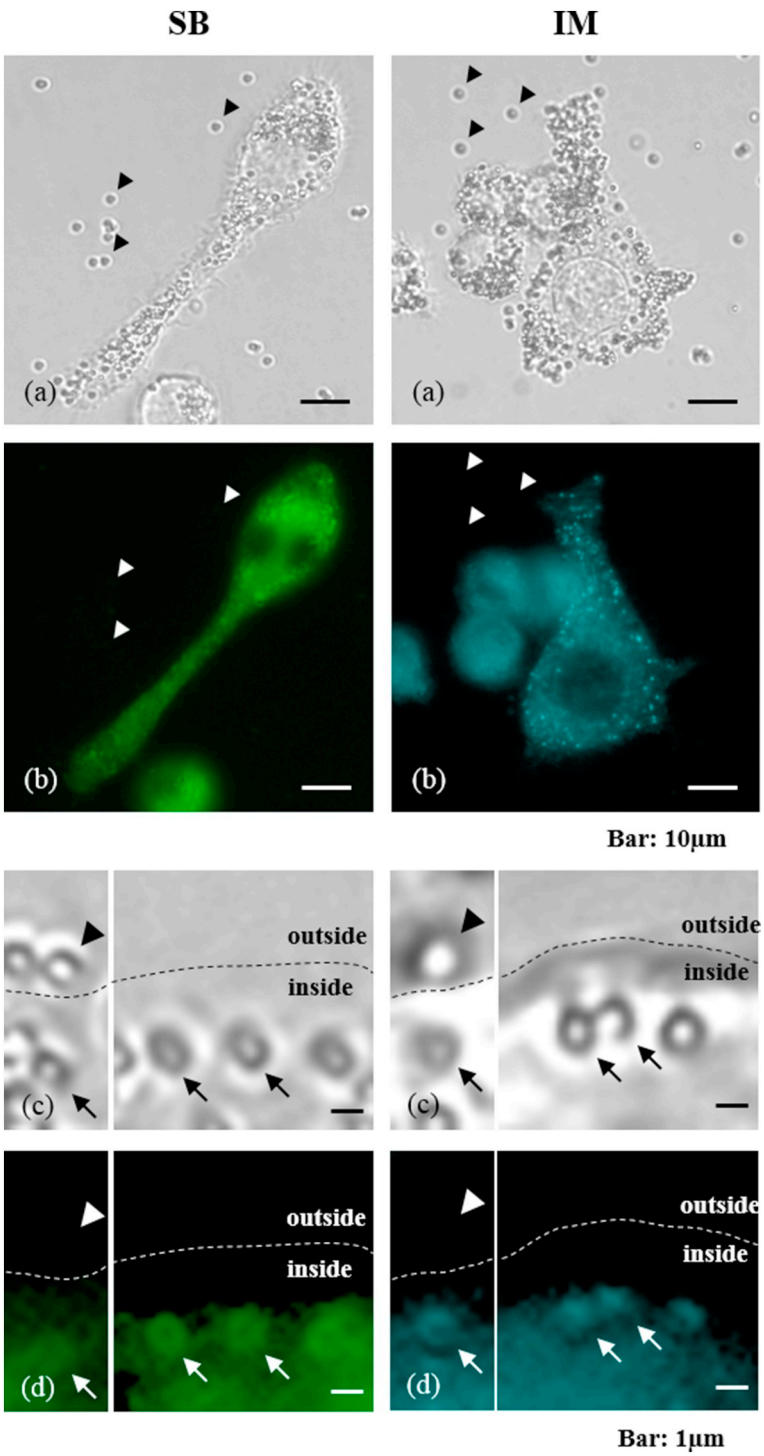

Fig. 12. Fluorescence images of hypochlorite-sensing probes in LPS-treated RAW264.7 cells phagocytosing non-fluorescent polystyrene beads. LPS-treated RAW264.7 cells were allowed to phagocytose polystyrene beads 1 μm in diameter for 30 min. The cells were then washed with PBS and incubated with 5×10^{-6} M **SB** or **IM**. Bright-field images (a, c); fluorescence images of RAW264.7 cells incubated with **SB** (left) and **IM** (right) (b, d). Arrowheads in (a-d) indicate: beads located outside of the cells; arrows in (c, d) indicate: beads located inside of the cells. Dashed line in (c, d) indicates locale of the cell membrane. Bars: 10 μm (a, b), 1 μm (c, d).

stimulated RAW264.7 cells with GSH (a scavenger of active oxygen species including hypochlorous acid) or taurine (a hypochlorite scavenger) strongly inhibited the fluorescence signal generated by **SB**. However, ABAH, GSH, and taurine were less effective in reducing fluorescence emission from the **IM** probe in PMA-stimulated cells compared with their effects on the **SB** probe in PMA-stimulated cells (Fig. 10, right).

In LPS-treated cells, the fluorescence signals emitted by **SB,** observed throughout the cytoplasm and as granule-like cellular structures (endosomes), were quenched by the addition of ABAH, GSH, and taurine (Fig. 11, left). With the **IM** probe, however, the inhibitory effects of ABAH, GSH, and taurine were restricted to the fluorescence signals detected as granule-like structures. Our results indicate that ABAH, GSH, and taurine did not inhibit the fluorescence signal

intensity of **IM**, which was observed throughout the cytoplasm (Fig. 11, right).

Our results show that **SB** is a fluorescent probe that is capable of visualizing hypochlorite endogenously generated by MPO in PMA- and LPS-treated RAW264.7 cells. **IM** is also suitable for the detection of hypochlorite generated in the endosomes formed by treatment with LPS. However, **IM** fluorescence, observed throughout the cytoplasm, was retained in PMA- and LPS-treated cells even after the addition of ABAH, GSH, and taurine. The mechanisms involved in the generation of **IM** fluorescence, observed in the cytoplasm of RAW264.7 cells, are still unclear; these mechanisms may be part of the sensing profile of the **IM** probe towards different ROS and anions. As shown in Fig. S15†, the **IM** probe showed relatively high background fluorescence and a noticeable, but not strong, fluorescent signal in the presence of peroxynitrate, hydroxyl radicals, and acetate. LPS can stimulate the production of various reactive chemical species such as $NO^{\bullet}$, $O_2^{\bullet -}$, $ONOO^-$, $^{\bullet}OH$, and HOBr (Fig. S28†) [61]. The **IM** probe may have been emitting fluorescence via reaction with certain reactive chemical species such as hydroxyl radicals; such species are generated by various mechanisms, including the Fenton reaction, and are not completely inhibited by GSH [62] and taurine [63].

3.12. Imaging of Hypochlorite Generation during Phagocytosis in LPS-Treated RAW264.7 Cells

Hypochlorite is generated during phagocytosis via release of hydrogen peroxide and myeloperoxidase; thus, we next investigated whether the probes **SB** and **IM** can be used for imaging hypochlorite generation during the process of phagocytosis. The fluorescence emitted by probes **SB** and **IM** in LPS-stimulated RAW 264.7 cells, incubated with non-fluorescent polystyrene beads (1 μm diameter), is shown in Fig. 12. After RAW 264.7 cells were incubated with the beads for 30 min, numerous beads were found on the cell surface, and some of the beads were integrated into the cells (Fig. 12). The beads found outside of the cells (Fig. 12a and b) and on the surface of the cells showed no fluorescence from the probes **SB** and **IM** (Fig. 12c and d). However, the beads integrated into the cells showed significant levels of fluorescence emitted by both probes (Fig. 12c and d).

These results show that the probes **SB** and **IM** can be used to monitor endogenously produced hypochlorite in endosomes and phagosomes during the processes of endocytosis in living cells.

4. Conclusion

In summary, we have developed the two probes, **SB** and **IM,** for selective and straightforward detection of ClO^- ions. The probes contain 4-diethylaminosalicylaldehyde moiety as the fluorophore; 4-diethylaminosalicylaldehyde is combined separately with 4-nitro-meta-phenylenediamine or 4-nitro-o-phenyenediamine, which serve as recognition units. These chromogenic and fluorogenic probes for the detection of ClO^- can be synthesized using simple one-step synthesis resulting in high yield. These probes show remarkable sensitivity, speedy response, and low limit of detection. In addition, the **SB** and **IM** probes can be used to monitor endogenously produced hypochlorite in endosomes of activated macrophages. These probes may provide a simple method to fabricate a biologically relevant chemical sensor.

Acknowledgement

Authors (RY, LM) thank UGC New Delhi and Banaras Hindu University, Varanasi, India for the financial assistance. We also acknowledge Dr. Ruchi Gaur, Department of Chemistry, Indian Institute of Technology, Kanpur, for X-ray crystallography data collection of **IM**.

Appendix A. Supplementary data

Supplementary data CCDC reference no. 1482721 and 1583949 contains the supplementary crystallographic data for **SB** and **IM** respectively. This data can be obtained free of charge via http://www.ccdc.cam.ac.uk/conts/retrieving.html, or from the Cambridge Crystallographic Data Centre, 12 Union Road, Cambridge CB2 1EZ, UK, fax: (+44) 1223–336-033, Supplementary data to this article can be found online at https://doi.org/10.1016/j.jphotobiol.2019.111594.

References

[1] C.C. Winterbourn, Reconciling the chemistry and biology of reactive oxygen species, Nat. Chem. Biol. (5) (2008) 278–286.
[2] (a) X. Zhen, C. Zhang, C. Xie, Q. Miao, K.L. Lim, K. Pu, Intraparticle energy level alignment of semiconducting polymer nanoparticles to amplify chemiluminescence for ultrasensitive in vivo imaging of reactive oxygen species, ACS Nano 10 (2016) 6400–6409;
(b) M. Valko, D. Leibfritz, J. Moncol, M.T.D. Cronin, M. Mazur, J. Telser, Free radicals and antioxidants in normal physiological functions and human disease, Int. J. Biochem. Cell Biol. 39 (2007) 44–84;
(c) D.I. Pattison, M.J. Davies, Absolute rate constants for the reaction of hypochlorous acid with protein side chains and peptide bonds, Chem. Res. Toxicol. 14 (2001) 1453–1464.
[3] C.C. Winterbourn, M.B. Hampton, J.H. Livesey, A.J. Kettle, Modeling the reactions of superoxide and myeloperoxidase in the neutrophil phagosome: implications for microbial killing, J. Biol. Chem. 281 (2006) 39860–39869.
[4] J.E. Harrison, J. Schultz, Studies on the chlorinating activity of myeloperoxidase, J. Biol. Chem. 251 (1976) 1371–1374.
[5] S.J. Klebanoff, Myeloperoxidase: friend and foe, J. Leukoc. Biol. 77 (2005) 598–625.
[6] D. Roos, C.C. Winterbourn, Immunology. Lethal weapons, Science 296 (2002) 669–671.
[7] V. Papayannopoulos, K.D. Metzler, A. Hakkim, A. Zychlinsky, Neutrophil elastase and myeloperoxidase regulate the formation of neutrophil extracellular traps, J. Cell Biol. 191 (2010) 677–691.
[8] E.A. Podrez, H.M. Abu-Soud, S.L. Hazen, Myeloperoxidase-generated oxidants and atherosclerosis, Free Radic. Biol. Med. 28 (2000) 1717–1725.
[9] S.M. Wu, S.V. Pizzo, α2-macroglobulin from rheumatoid arthritis synovial fluid: functional analysis defines a role for oxidation in inflammation, Arch. Biochem. Biophys. 391 (2001) 119–126.
[10] J. Himmelfarb, Relevance of oxidative pathways in the pathophysiology of chronic kidney disease, Cardiol. Clin. 23 (2005) 319–330.
[11] S. Hammerschmidt, T. Vogel, S. Jockel, C. Gessner, H.J. Seyfarth, A. Gillissen, H. Wirtz, Protein kinase C inhibition attenuates hypochlorite-induced acute lung injury, Resp. Med. 101 (2007) 1205–1211.
[12] C.J. Venglarik, J. Giron-Calle, A.F. Wigley, E. Malle, N. Watanabe, H.J. Forman, Hypochlorous acid alters bronchial epithelial cell membrane properties and prevention by extracellular glutathione, J. Appl. Physiol. 95 (2003) 2444–2452.
[13] I. Rahman, S.K. Biswas, L.A. Jimenez, M. Torres, H.J. Forman, Glutathione, stress responses, and redox signaling in lung inflammation, Antioxid. Redox Signal. 7 (2005) 42–59.
[14] Y.Q. Gong, B. Yu, W. Yang, X.L. Zhang, Phosphorus, and nitrogen co-doped carbon dots as a fluorescent probe for real-time measurement of reactive oxygen and nitrogen species inside macrophages, Biosens. Bioelectron. 79 (2016) 822–828.
[15] S. Thiagarajan, Z.Y. Wu, S.M. Chen, Amperometric determination of sodium hypochlorite at poly MnTAPP-nano Au film modified electrode, J. Electroanal. Chem. 661 (2011) 322–328.
[16] S.S. Ding, Q. Zhang, S.H. Xue, G.Q. Feng, Real-time detection of hypochlorite in tap water and biological samples by a colorimetric, ratiometric and near-infrared fluorescent turn-on probe, Analyst 140 (2015) 4687–4693.
[17] H.L. Gong, Y. Jiang, R.C. Hou, X.Q. Ding, A sensitive and selective fluorescent coumarin-based probe for detection of hypochlorite ion and its application to cellular imaging, J. Fluoresc. 26 (2016) 403–406.
[18] D. Wu, A.C. Sedgwick, T. Gunnlaugsson, E.U. Akkaya, J. Yoon, T.D. James, Fluorescent chemosensors: the past, present and future, Chem. Soc. Rev. 46 (2017) 7105–7123.
[19] Y. Yang, Q. Zhao, W. Feng, F. Li, Luminescent chemodosimeters for bioimaging, Chem. Rev. 113 (2013) 192–270.
[20] W. Xu, Z. Zeng, J.H. Jiang, Y.T. Chang, L. Yuan, Discerning the chemistry in individual organelles with small-molecule fluorescent probes, Angew. Chem. Int. Ed. 55 (2016) 13658–13699.
[21] M. Vendrell, D. Zhai, J.C. Er, Y.T. Chang, Combinatorial strategies in fluorescent probe development, Chem. Rev. 112 (2012) 4391–4420.
[22] W. Sun, S. Guo, C. Hu, J. Fan, X. Peng, Recent development of chemosensors based on cyanine platforms, Chem. Rev. 116 (2016) 7768–7817.
[23] D. Oushiki, H. Kojima, T. Terai, M. Arita, K. Hanaoka, Y. Urano, T. Nagano, Development and application of a near-infrared fluorescence probe for oxidative stress based on differential reactivity of linked cyanine dyes, J. Am. Chem. Soc. 132 (2010) 2795–2801.
[24] G.H. Cheng, J.L. Fan, W. Sun, K. Sui, X. Jin, J.Y. Wang, X.J. Peng, A highly specific

BODIPY-based probe localized in mitochondria for HClO imaging, Analyst 138 (2013) 6091–6096.
[25] X. Xu, Y. Qian, A novel (3, 6-di-tert-butylcarbazol-9-yl) triphenylamine–BODIPY–tricyanofuran conjugated dye: synthesis and rapid naked-eye detection of hypochlorite, New J. Chem. 41 (2017) 9607–9612.
[26] Q.L. Xu, C.H. Heo, G. Kim, H.W. Lee, H.M. Kim, J. Yoon, Development of imidazoline-2-thiones based two-photon fluorescence probes for imaging hypochlorite generation in a co-culture system, Angew. Chem. Int. Ed. 54 (2015) 4890–4894.
[27] F.B. Yu, P. Li, P. Song, B.S. Wang, J.Z. Zhao, K.L. Han, Facilitative functionalization of cyanine dye by an on-off-on fluorescent switch for imaging of H_2O_2 oxidative stress and thiols reducing repair in cells and tissues, Chem. Commun. 48 (2012) 4980–4982.
[28] D.N. Dhar, C.L. Taploo, Schiff bases and their applications, J. Sci. Ind. Res. 41 (1982) 501–506.
[29] P. Przybylski, A. Huczynski, K. Pyta, B. Brzezinski, F. Bartl, Biological properties of Schiff bases and azo derivatives of phenols, Curr. Org. Chem. 13 (2009) 124–148.
[30] M.B. Halli, R.S. Malipatil, R.B. Sumathi, K. Shivakumar, Synthesis, spectroscopic characterization and biological activity studies of schiff base metal complexes derived from N'- (4-(methylthio) benzylidene) benzofuran- 2-carbohydrazide, Pharm. Lett. 5 (2013) 182–188.
[31] M. Shibata, T. Tanimoto, H. Kandori, Water molecules in the Schiff Base region of bacteriorhodopsin, J. Am. Chem. Soc. 125 (2003) 13312–13313.
[32] L. Li, Z. Li, K. Wang, S. Zhao, J. Feng, J. Li, P. Yang, Y. Liu, L. Wang, Y. Li, H. Shang, Q. Wang, Design, synthesis, antiviral activity, and structure–activity relationships (SARs) of two types of structurally novel phenanthroindo/quinolizidine analogues, J. Agric. Food Chem. 62 (6) (2014) 11080–11088.
[33] M. Gulcan, M. Sonmez, I. Berber, Synthesis, characterization, and antimicrobial activity of a new pyrimidine Schiff base and its Cu(II), Ni(II), Co(II), Pt(II), and Pd (II) complexes, Turk. J. Chem. 36 (2012) 189–200.
[34] K.F. Ansari, C. Lal, Synthesis, physicochemical properties and antimicrobial activity of some new benzimidazole derivatives, Eur. J. Med. Chem. 44 (2009) 4023–4028.
[35] M. Alp, H. Goker, R. Brun, S. Yildiz, Synthesis and antiparasitic and antifungal evaluation of 2′-arylsubstituted-1H,1′H-[2,5′]bisbenzimidazolyl-5-carboxamidines, Eur. J. Med. Chem. 44 (2009) 2002–2008.
[36] M. Sunitha, P. Jogi, B. Ushaaiah, C. Gyanakumari, Synthesis¸ structural characterization, molecular modelling and antimicrobial studies of transition metal complexes of schiff base ligand derived from 5-chlorosalicylaldehyde and 2-(2-aminophenyl) 1H-benzimidazole, J. Chem. Pharm. Res. 4 (2012) 1553–1561.
[37] Y. Garg, M.K. Samota, G. Seth, Synthesis and antifungal activity of some metal complexes of 2-(2'-Hydroxybenzylidene)aminophenyl benzimidazole, Asian J. Chem. 17 (2005) 615–617.
[38] J.S. Derrick, A.K. Richard, K.J. Korshavn, M.J. McLane, J. Kang, E. Nam, A. Ramamoorthy, B.T. Ruotolo, M.H. Lim, Importance of the dimethylamino functionality on a multifunctional framework for regulating metals, amyloid-β, and oxidative stress in Alzheimer's disease, Inorg. Chem. 55 (2016) 5000–5013.
[39] S. Samanta, S. Halder, P. Dey, U. Manna, A. Ramesh, G. Das, Ratiometric fluorogenic probe for real-time detection of SO_3^{2-} in aqueous medium: application in cellulose paper based device and potential to sense in mitochondria, Analyst 143 (2018) 250–257.
[40] G.M. Sheldrick, Acta Crystallogr. Sect. C. Struct. Chem. 71 (2015) 3–8.
[41] M.J. Frisch, G.W. Trucks, G.E. Scuseria, H.B. Schlegel, M.A. Robb, J.R. Cheeseman, V. Barone, G. Scalmani, B. Mennucci, G.A. Petersson, H. Nakatsuji, M. Caricato, X. Li, H.P. Hratchian, A.F. Izmaylov, J. Bloino, G. Zheng, J.L. Sonnenberg, M. Hada, M. Ehara, K. Toyota, R. Fukuda, J. Hasegawa, M. Ishida, T. Nakajima, Y. Honda, O. Kitao, H. Nakai, T. Vreven, J.A. Montgomery Jr., J.E. Peralta, F. Ogliaro, M. Bearpark, J.J. Heyd, E. Brothers, K.N. Kudin, V.N. Staroverov, R. Kobayashi, J. Normand, K. Raghavachari, A. Rendell, J.C. Burant, S.S. Iyengar, J. Tomasi, M. Cossi, N. Rega, J.M. Millam, M. Klene, G.A. Voth, J.E. Knox, J.B. Cross, V. Bakken, C. Adamo, J. Jaramillo, R. Gomperts, R.E. Stratmann, O. Yazyev, A.J. Austin, R. Cammi, C. Pomelli, J.W. Ochterski, R.L. Martin, K. Morokuma, V.G. Zakrzewski, P. Salvador, J.J. Dannenberg, S. Dapprich, A.D. Daniels, O. Farkas, J.B. Foresman, J.V. Ortiz, J. Cioslowski, D.J. Fox, Gaussian 09, Revision A.02, Gaussian Inc., Wallingford, CT, 2009.
[42] V.S. Padalkar, V.S. Patil, V.D. Gupta, K.R. Phatangare, P.G. Umape, N. Sekar, Synthesis, characterization, thermal properties, and antimicrobial activities of 5-(diethylamino)-2-(5-nitro-1H-benzimidazol-2-yl) phenol and its transition metal complexes, ISRN Org. Chem. (2011) (Article ID 738361).
[43] X. Xu, Y. Qian, A novel (3, 6-di-tert-butylcarbazol-9-yl) triphenylamine–BODIPY–tricyanofuran conjugated dye: synthesis and rapid naked-eye detection of hypochlorite, New J. Chem. 41 (2017) 9607–9612.
[44] K. Setsukinai, Y. Urano, K. Kakinuma, H.J. Majima, T.J. Nagano, Biol. Chem. 278 (2003) 3170–3175.
[45] J. Li, C. Yin, Y. Wen, F. Huo, A new mechanism-based fluorescent probe for the detection of ClO^- by UV–vis and fluorescent spectra and its applications, Sens. Actuators B Chem. 252 (2017) 1112–1117.
[46] U. Stoin, A.I. Shames, I. Malka, I. Bar, Y. Sasson, Chem. Phys. Chem. 14 (2013) 4158–4164.
[47] M.H. Zou, V. Ullrich, FEBS Lett. 382 (1996) 101–104.
[48] A.M. Held, D.J. Halko, J.K. Hurst, J. Am. Chem. Soc. 100 (1978) 5732–5740.
[49] A. Hakonen, Plasmon enhancement and surface wave quenching for phase ratiometry in coextraction-based fluorosensors, Anal. Chem. 81 (2009) 4555–4559.
[50] A.J. Kettle, C.A. Gedye, C.C. Winterbourn, Mechanism of inactivation of myeloperoxidase by 4-aminobenzoic acid hydrazide, Biochem. J. 321 (1997) 503–508.
[51] G.R. Haenen, A. Bast, Glutathione revisited: a better scavenger than previously thought, Front. Pharmacol. 5 (2014) 260.
[52] D.B. Learn, V.A. Fried, E.L. Thomas, Taurine and hypotaurine content of human leukocytes, J. Leukoc. Biol. 48 (1990) 174–182.
[53] R. Yadav, K. Odera, A. Rai, A. Noguchi, R. Takahashi, L. Mishra, A stable and highly sensitive fluorescent probe for detection of hypochlorite ion in vitro and in living cells, Chem. Lett. 48 (2019) 110–113.
[54] J.W. Li, C.X. Yin, T. Liu, Y. Wen, F.J. Huo, A new mechanism-based fluorescent probe for the detection of ClO^- by UV–vis and fluorescent spectra and its applications, Sens. Actuators. B Chem. 252 (2017) 1112–1117.
[55] V. Delgado-Rizo, M.A. Martínez-Guzmán, L. Iñiguez-Gutierrez, A. García-Orozco, A. Alvarado-Navarro, M. Fafutis-Morris, Neutrophil extracellular traps and its implications in inflammation: an overview, Front. Immunol. 8 (2017) 81.
[56] A. Karlsson, J.B. Nixon, L.C. McPhail, Phorbol myristate acetate induces neutrophil NADPH-oxidase activity by two separate signal transduction pathways: dependent or independent of phosphatidylinositol 3-kinase, J. Leukoc. Biol. 67 (2000) 396–404.
[57] S.E. Gomez-Mejiba, Z. Zhai, M.S. Gimenez, M.T. Ashby, J. Chilakapati, K. Kitchin, R.P. Mason, D.C. Ramirez, Myeloperoxidase-induced genomic DNA-centered radicals, J. Biol. Chem. 285 (2010) 20062–20071.
[58] S.M. Tse, W. Furuya, E. Gold, A.D. Schreiber, K. Sandvig, R.D. Inman, S. Grinstein, Differential role of actin, clathrin, and dynamin in Fc gamma receptor-mediated endocytosis and phagocytosis, J. Biol. Chem. 278 (2003) 3331–3338.
[59] R.E. Harrison, C. Bucci, O.V. Vieira, T.A. Schroer, S. Grinstein, Phagosomes fuse with late endosomes and/or lysosomes by extension of membrane protrusions along microtubules: role of Rab7 and RILP, Mol. Cell. Biol. 23 (2003) 6494–6506.
[60] D.C. Klein, A. Skjesol, E.D. Kers-Rebel, T. Sherstova, B. Sporsheim, K.W. Egeberg, B.T. Stokke, T. Espevik, H. Husebye, CD14, TLR4 and TRAM show different trafficking dynamics during LPS stimulation, Traffic 16 (2015) 677–690.
[61] I.L. Chapple, J.B. Matthews, The role of reactive oxygen and antioxidant species in periodontal tissue destruction, Periodontol. 43 (2007) (2000) 160–232.
[62] N. Spear, S.D. Aust, Effects of glutathione on Fenton reagent-dependent radical production and DNA oxidation, Arch. Biochem. Biopys. 324 (1995) 111–116.
[63] O.I. Aruoma, B. Halliwell, B.M. Hoey, J. Butler, The antioxidant action of taurine, hypotaurine and their metabolic precursors, Biochem. J. 256 (1988) 251–255.